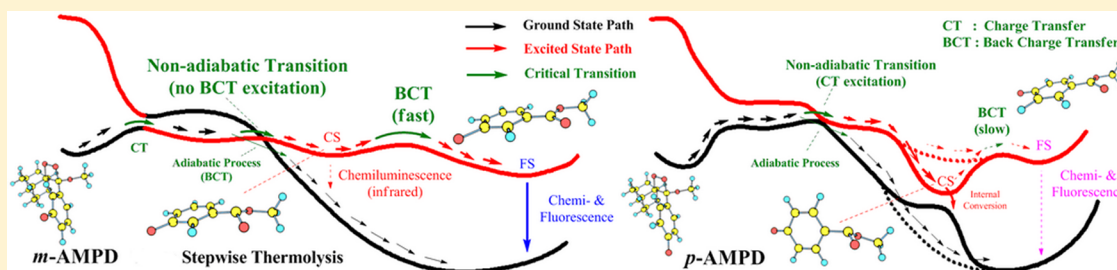


Mechanism of AMPPD Chemiluminescence in a Different Voice

Ling Yue and Ya-Jun Liu*

Key Laboratory of Theoretical and Computational Photochemistry, Ministry of Education, College of Chemistry, Beijing Normal University, Beijing 100875, China

S Supporting Information



ABSTRACT: The chemiluminescence phenomenon of 3-(2'-spiroadamantyl)-4-methoxy-4-(3''-phosphoryloxy)-phenyl-1,2-dioxetane (AMPPD or *m*-AMPPD) has been routinely applied in clinical diagnostics. Although the AMPPD chemiluminescence immunoassay is one of the most successful immunoassays, the mechanism of AMPPD chemiluminescence remains largely unknown. The AMPPD chemiluminescence process is composed of three steps: AMPPD is enzymatically triggered to produce 3-(2'-spiroadamantyl)-4-methoxy-4-(3''-hydroxyphenyl)-1,2-dioxetane (*m*-AMPD); *m*-AMPD decomposes into the excited-state methyl *m*-oxybenzoate anion (*m*-MOB[−]); the excited-state *m*-MOB[−] relaxes to its ground state and emits light. Obviously, the middle step is critical for the chemiluminescence and has not been well understood because of both experimental and theoretical difficulties. We performed the first theoretical study on the chemiluminescent decomposition mechanism of *m*-AMPD and its *para* isomer, *p*-AMPD, using the complete active space self-consistent field and the second-order multiconfigurational perturbation methods in addition to the density functional method. This investigation revealed that (1) neither the intramolecular chemical initiated electron exchange luminescence (CIEEL) nor the concerted charge transfer (CT) mechanism can describe the decomposition of *m*- and *p*-AMPD well. Instead, their decomposition occurs according to our previously proposed mechanism of gradually reversible CT-initiated luminescence. (2) The different stabilities of the *m*- and *p*-AMPD chemiexcited states might be the basis for the large difference in their chemiluminescence efficiencies. (3) The relationship between the chemiluminescence efficiency and the position of the electron donor on the aromatic ring, the so-called "odd/even selection rule," does not fully explain the chemiluminescence efficiency of dioxetanes. The odd/even selection rule is only correct for partial dioxetanes, because it does not capture the origin of the relationship between the chemiluminescence and the donor. We revealed that the origin consists of a combination of conjugation, induction, and steric effects. On the basis of this combination of effects, we theoretically designed some 1,2-dioxetanes to guide experimentalists in the synthesis of these excellent chemiluminescent molecules.

■ INTRODUCTION

The 1,2-dioxetanes are important organic chemiluminescent substrates because their thermolysis efficiently produces excited-state carbonyl products, which subsequently emit light.^{1–5} However, most 1,2-dioxetanes have vanishingly short lifetimes at room temperature, which limited their practical application until the synthesis of 3-(2'-spiroadamantyl)-4-methoxy-4-(3''-phosphoryloxy)-phenyl-1,2-dioxetane (AMPPD or *m*-AMPPD, *m*-AMPPD is used in this paper) in 1988.^{6–8} *m*-AMPPD is rather stable and hardly decomposes in the solid phase under low temperatures.^{9,10} The hydrolysis of AMPPD without the aid of enzyme catalysis is very slow, but an alkaline phosphatase (ALP) catalyst can rapidly decompose AMPPD to radiate visible light effectively. The enzymatically induced chemiluminescent decomposition of AMPPD has proven to be a valuable tool in diagnostic clinical

applications.^{1,5,7–9,11,12} *m*-AMPPD has been used in direct assays for enzymes and DNA and immunoassays for proteins, haptens, and microorganisms.^{8,9,13} *m*-AMPPD is also used in various photosensitive detection devices, such as photomultipliers and X-ray films, due to the strong signal and low background.⁸

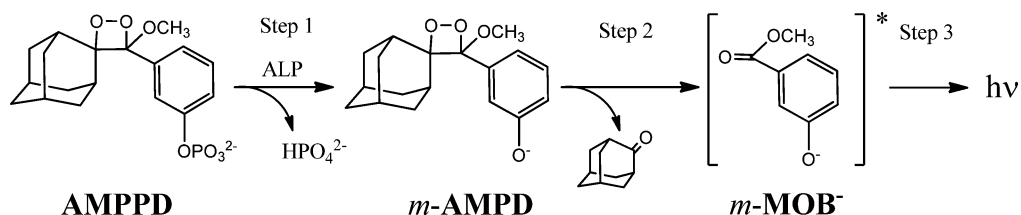
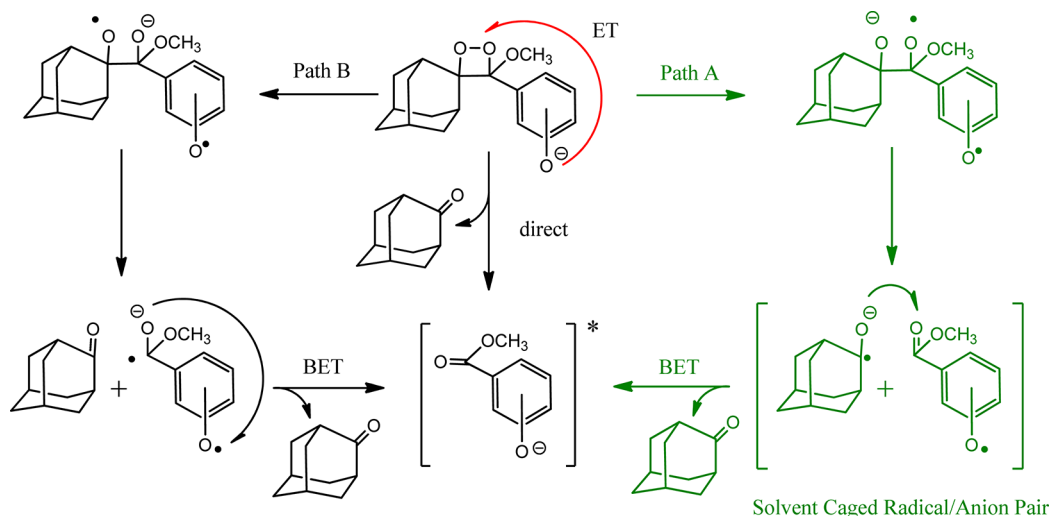
The *m*-AMPPD chemiluminescence (CL) process consists of three steps⁸ as shown in Scheme 1. First, *m*-AMPPD hydrolysis is catalyzed by ALP, and an extremely unstable intermediate (Int), 3-(2'-spiroadamantyl)-4-methoxy-4-(3''-hydroxyphenyl)-1,2-dioxetane (*m*-AMPD), is produced. Second, *m*-AMPD decomposes quickly into a ground-state (*S*₀) adamantone and a methyl *m*-oxybenzoate anion (*m*-MOB[−]), which is partially in

Received: March 14, 2013

Published: April 15, 2013



Scheme 1. Chemiluminescence Process of AMPPD

Scheme 2. The Assumed Intramolecular CIEEL and CT/Direct Mechanisms for *m*- and *p*-AMPD

the excited state and partially in the ground state. Finally, the excited-state *m*-MOB[−] relaxes to its *S*₀ state and emits light. However, the detailed CL mechanism of *m*-AMPPD is still not well understood, especially at the molecular and electronic-state level. Experimentally, the decomposition process cannot be directly observed because the active Int, *m*-AMPD, is difficult to synthesize,¹⁴ and the transition state (TS) and charge population cannot be detected. Theoretically, the surely existing biradical (or biradicaloid) and nearly degenerated states during the *m*-AMPD thermolysis^{15–25} are considerable challenges.

The *m*-AMPD thermolysis is obviously the most critical step in the *m*-AMPPD CL process. Understanding the *m*-AMPD thermolysis leading to the excited-state *m*-MOB[−] (*m*-MOB^{−*}) is the key to uncovering the AMPPD CL mechanism. The *m*-AMPD thermolysis has a high chemiluminescence efficiency and singlet chemiexcitation yield (Φ^{CL} and Φ^{S} are more than 25% and 50%, respectively, in aprotic organic solvents).^{1,2,26} Intramolecular chemical-initiated electron exchange luminescence (intramolecular CIEEL)^{27,28} was proposed to be the mechanism of the chemiluminescent decomposition (see Scheme 2). This mechanism assumes that the decomposition is first initiated by electron transfer (ET) from the electron donor (phenolic moiety) to the peroxide bond, forming a solvent-caged neutral radical/anionic radical pair (path A) or anionic biradical (path B). Then a subsequent intermolecular back ET (BET) between the radicals or an intramolecular BET releases enough energy to excite the fluorophore (*m*-MOB[−]) to its first singlet excited state (*S*₁). Adam et al.^{28,29} measured the viscosity dependence of the CL yield of *m*-AMPPD and its regioisomer, 3-(2'-spiroadamantyl)-4-methoxy-4-(4"-phosphoryloxy)-phenyl-1,2-dioxetane (*p*-AMPPD), and suggested that the chemiluminescent decomposition of *m*- and *p*-AMPPD

occurs via an intramolecular ET and an intermolecular BET process as in path A in Scheme 2. In addition to the stepwise intramolecular CIEEL mechanism, a concerted mechanism, such as the charge transfer/direct (CT/direct)^{30–33} (Scheme 2) and charge transfer induced luminescence (CTIL)^{18,23} mechanisms, was also proposed to explain this type of CT-induced decomposition because the existence and efficiency of a BET excitation between radicals in a solvent cage is questionable.^{18,23,30,31,33}

In addition to the questions still surrounding the thermolysis mechanism of *m*-AMPD, the difference in the chemiexcited emitter (the chemiexcited-state (CS) *m*-MOB[−] anion from the decomposition that emits the initial CL) and the photoexcited emitter (the photoexcited *m*-MOB[−] anion that emits fluorescence (FL)) was never previously considered. Roca-Sanjuán et al. recently revealed the difference between the CS and the photoexcited state (i.e., fluorescent state (FS)) using CASSCF/CASPT2 calculations on a small model of coelenteramide and Cypridina oxyluciferin.³⁴ The experimentally observed maxima^{9,10,13} of the AMPPD CL (i.e., AMPD CL, see Scheme 1) and the FL of *m*-MOB[−] (the decomposition product of AMPPD, see Scheme 1) are nearly the same in aprotic solvents.^{9,10,13} To fully understand the AMPD CL and the *m*-MOB[−] FL, we have to understand the difference between the CS and FS of *m*-MOB[−].

The third obstacle to understanding the chemiluminescent mechanism of the AMPPD is the effect of the regioselectivity of the substituent, the so-called "odd/even selection rule."^{28,29} It was found that *m*-AMPD exhibited a steady-state glow for several minutes (2–30 min depending on its immediate environment) while its *para* analog exhibited a flash luminescence during the chemiluminescent decomposition.^{7,28,29,35,36} The relationship between the luminescent

efficiency and position of the electron donor on the aromatic ring was named the “odd/even selection rule” and was also observed for other adamantylidenedioxetanes with naphthyl,^{37,38} siloxynaphthalen-2-yl,^{37,39–41} siloxybenzo(b)furan-2-yl,⁴² and siloxybenzo(b)thiophen-2-yl⁴² substituents and for some bicyclic 1,2-dioxetanes with a 2-hydroxynaphthyl substituent.⁴³ For these 1,2-dioxetanes bearing an aromatic-ring substituent, the even-pattern substituted isomer (like *p*-AMPD) has a faster decay rate but lower CL efficiency than the odd-pattern substituted isomer (like *m*-AMPD). Adam and Trofimov simply attributed the higher luminescent efficiency of *m*-AMPD compared to that of *p*-AMPD to the higher excitation energy of the methyl *p*-oxybenzoate anion (*p*-MOB[−]) during the BET process based on their proposed intramolecular CIEEL mechanism.²⁸ However, the solvent-caged radical/anion pair and the complete electron transfer/back electron transfer (ET/BET) process in the intramolecular CIEEL mechanism are not observed directly in the experiments. Moreover, the inability of the intramolecular CIEEL mechanism to explain the dramatic difference in the luminescence yields (ca. 10⁴-fold!) of *m*- and *p*-AMPD is obvious.²⁸ In addition, McCapra³² qualitatively explained the odd/even selection rule using an orbital picture that showed how charge transfer (CT) enhances the formation of the excited state based on the assumption of concerted decomposition. Other similar explanations of the orbital interactions based on the concerted CTIL^{18,23} and the infrared radiation⁴⁴ mechanisms were all derived from simple model molecules of adamantylidenedioxetane or bicyclic dioxetane. It is unclear whether the odd/even selection rule can extend to all 1,2-dioxetanes bearing an aromatic-ring substituent. The origin of the odd/even selection rule is also unknown. These issues must be addressed to understand the factors affecting the CL efficiency of all 1,2-dioxetanes.

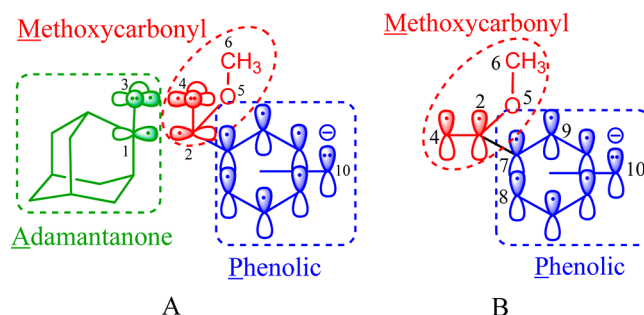
In summary, to understand the CL mechanism of AMPPD, the following aspects need to be investigated: (1) the thermolysis processes of *m*-AMPD and *p*-AMPD leading to the excited-state *m*-MOB[−] and *p*-MOB[−] anions, respectively, (2) the differences in the CS and FS of *m*-MOB[−] and *p*-MOB[−], and (3) the origin of the odd/even selection rule. The purpose of this paper is to solve these three problems, which are related not only to the CL of AMPPD but also to the CL of all 1,2-dioxetanes. We employed single configurational and multi-configurational methods to address the issues by qualitatively simulating the AMPPD chemiluminescent decomposition process and elucidating the CL mechanism. This theoretical work will be helpful in designing more efficient CL substrates.

■ COMPUTATIONAL DETAILS

We investigated the thermolysis mechanisms of *m*-AMPD and *p*-AMPD using a combination of a multiconfigurational approach and density functional theory (DFT). This combined method was successfully used to study the chemiluminescent decomposition of the phenolic-substituted 1,2-dioxetanone²³ and the firefly dioxetanone.²⁴ The Coulomb-attenuated hybrid exchange-correlation functional (CAM-B3LYP),⁴⁵ which was designed to describe CT excitations more accurately,^{46,47} was employed. The unrestricted open shell CAM-B3LYP (UCAM-B3LYP) method with broken-symmetry (BS) technology was employed to calculate the intrinsic reaction coordinate (IRC),^{48,49} optimize the stationary points (i.e., the minimum (Min), TS, and Int), and analyze the frequencies of the ground states of these points. The Mulliken population analysis was

employed to elucidate the CT characteristics. The 6-31G** basis set^{50,51} was employed for all of the CAM-B3LYP calculations. The larger 6-31+G** basis set was tested, and no improvement in the results was observed. To investigate the energetics, single-point calculations on the CAM-B3LYP optimized ground-state geometries of gas-phase *m*- and *p*-AMPD were performed using the multistate second-order multiconfigurational perturbation (MS-CASPT2)^{52–54} method. To include all of the relevant electronic states, six roots with equal weights were calculated using the state-averaged complete active space self-consistent field (SA-CASSCF)^{55,56} method. However, only the three lowest singlet states are relevant for the CL. Therefore, the results for the higher states are not shown here. The 16-in-13 active space which includes all π/π^* orbitals on the phenolic moiety, C₁–C₂ σ/σ^* orbitals, O₃–O₄ σ/σ^* orbitals, and p orbitals on the two oxygens in the four-member ring moiety, were chosen for *m*- and *p*-AMPD (see Chart 1A). The ANO-RCC basis set⁵⁷ with a contraction

Chart 1. The 16-in-13 Active Space and Partial Atomic Labels for *m*- and *p*-AMPD (A) and the 10-in-9 Active Space and Partial Atomic Labels for *m*- and *p*-MOB[−] (B)



scheme of [3s2p1d] for carbon, nitrogen, and oxygen; [4s3p1d] for sulfur; and [2s1p] for hydrogen (denoted as ANO-RCC-VDZP) was employed in the MS-CASPT2 calculations. All of these DFT calculations were performed using the Gaussian 09 program suite.⁵⁸ The MS-CASPT2 single-point calculations were performed using MOLCAS 7.6.⁵⁹

The stationary points for the gas-phase S₁ state of both *m*-MOB[−] and *p*-MOB[−] were optimized using the SA-CASSCF method. Numerical vibrational analyses using forward differences and the quadratic steepest descent (QSD) reaction path following^{60,61} method were performed at the same level of theory to confirm that the TS had been located. The CASPT2 single-point energy correction was also performed for the SA-CASSCF optimized geometries. Meanwhile, to simulate the experimental environment,⁴⁰ the conductor-like polarized continuum model (C-PCM)⁶² was used to capture solvent effects. The polar solvents, DMSO, and water (the dielectric constants, ϵ , are 46.70 and 78.39, respectively) were employed in the self-consistent reaction field calculations. The 10-in-9 active space, which includes all of the π/π^* orbitals (see Chart 1B), and two roots with equal weights were used for the SA-CASSCF geometry optimizations. The 6-31G** basis set^{50,51} was used in the SA-CASSCF optimizations. The ANO-RCC-VDZP basis set was used in the CASPT2 calculations. All of the SA-CASSCF optimizations were performed with MOLPRO 2010,⁶³ and the CASPT2 single-point energy corrections both in the gas phase and in the solvents were calculated using MOLCAS 7.6.⁶⁴

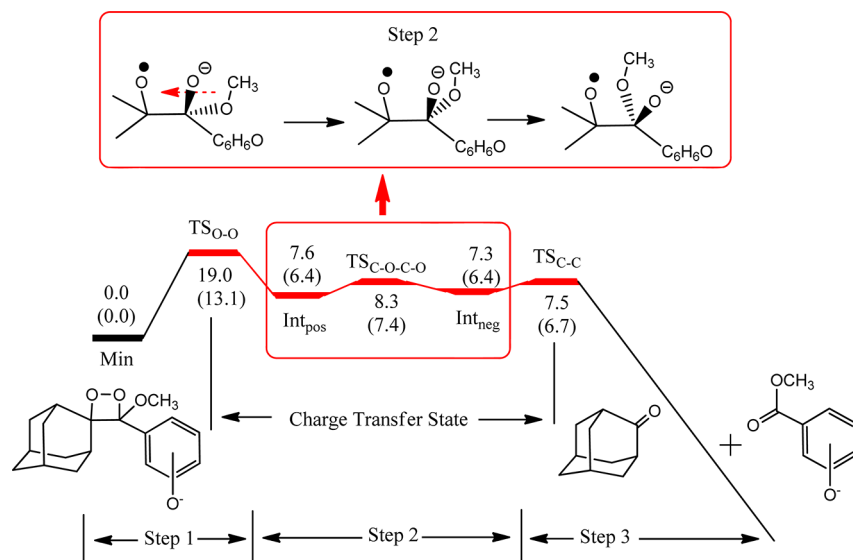


Figure 1. The Gibbs free energy profile (kcal/mol) for the decomposition of *m*-AMPD and *p*-AMPD (in parentheses) calculated at the CAM-B3LYP/6-31G** level.

RESULTS

One minimum (Min) for the reactant, three TSs, and two Ints were located for the ground-state decomposition of both *m*-AMPD and *p*-AMPD by the CAM-B3LYP method. The Min is denoted as *m*- and *p*-Min for *m*- and *p*-AMPD, respectively. On the basis of the imaginary vibrational modes, the three TSs correspond to the breaking of the O₃–O₄ bond, the rotation of the C₆–O₅–C₂–O₄ dihedral angle, and the breaking of the C₁–C₂ bond. Therefore, we refer to them as *m*-TS_{O–O} (*p*-TS_{O–O}), *m*-TS_{C–O–C–O} (*p*-TS_{C–O–C–O}), and *m*-TS_{C–C} (*p*-TS_{C–C}), respectively, for *m*-AMPD (*p*-AMPD). The two Int structures are of a positive and a negative C₆–O₅–C₂–O₄ dihedral angle and are denoted as *m*-Int_{pos} (*p*-Int_{pos}) or *m*-Int_{neg} (*p*-Int_{neg}), respectively, for *m*-AMPD (*p*-AMPD; see Figure 1 for the energy profile). In order to describe the CT characteristics of the excited states, *m*- and *p*-AMPD were divided into three parts: the adamantanone (A), methoxycarbonyl (M), and phenolic (P) moieties (see Chart 1A). The important geometric parameters of the CAM-B3LYP optimized structures and the relative single-point energies of the adiabatic S₀ and S₁ states at the MS-CASPT2 level are listed in Tables 1 and 2, respectively. The Mulliken charge of the A, M, and P moieties for these stationary points calculated at the CAM-B3LYP and CASPT2 levels are summarized in Table 3. The most important natural orbitals (NO) and the corresponding occupation numbers of these stationary points calculated with the CAM-B3LYP method are shown in Figures S1 and S2, respectively. The pseudo-NO and its occupation number for the S₀, S₁, and S₂ states calculated at the SA-CASSCF level of theory are shown in Figures S3–S14. The Mulliken charge populations on the three moieties of *m*- and *p*-AMPD together with the S₀ potential energy curves (PECs) and the changes in the critical geometric parameters at the CAM-B3LYP/6-31G** level are shown in Figure S15. For convenience, the approximate diabatic states will be used in the Discussion section below. From the natural orbital analyses performed with CAM-B3LYP (Figures S1 and S2) and SA-CASSCF (Figures S3–S14), the Mins and the S₀ products from the O₃–O₄ and C₁–C₂ bond cleavages for *m*- and *p*-AMPD mainly correspond to a typical Hartree–Fock closed-shell configuration. We

Table 1. The Important Bonds (Å) and Dihedral Angles (deg) of the *m*- and *p*-AMPD Stationary Points Optimized at the CAM-B3LYP/6-31G** Level^a

stationary point	bond length				dihedral angle	
	C ₁ –C ₂	O ₃ –O ₄	C ₁ –O ₃	C ₂ –O ₄	O ₃ –C ₁ –C ₂ –O ₄	C ₆ –O ₅ –C ₂ –O ₄
<i>m</i> -Min	1.551	1.465	1.459	1.446	11.3	64.0
<i>m</i> -TS _{O–O}	1.550	1.807	1.427	1.383	18.0	47.2
<i>m</i> -Int _{pos}	1.557	2.134	1.405	1.338	32.5	32.2
<i>m</i> -TS _{C–O–C–O}	1.557	2.142	1.406	1.338	35.2	16.2
<i>m</i> -Int _{neg}	1.557	2.150	1.406	1.340	36.4	–28.9
<i>m</i> -TS _{C–C}	1.604	2.448	1.392	1.301	51.2	–18.3
<i>p</i> -Min	1.560	1.468	1.455	1.452	9.8	62.6
<i>p</i> -TS _{O–O}	1.567	1.789	1.412	1.384	15.3	42.9
<i>p</i> -Int _{pos}	1.560	2.125	1.400	1.341	30.8	31.6
<i>p</i> -TS _{C–O–C–O}	1.560	2.133	1.402	1.342	33.5	12.5
<i>p</i> -Int _{neg}	1.560	2.136	1.403	1.344	33.9	–29.1
<i>p</i> -TS _{C–C}	1.604	2.417	1.390	1.308	47.6	–19.5

^aSee Chart 1 for the atomic labels.

denoted the diabatic state on the S₀ PEC as closed-shell/¹(σ,σ*). During the decomposition, the S₁ state changes from (π,π*) to (π,σ*) as in a typical CT process. Therefore, we referred to the diabatic state on the S₁ PEC as ¹(π,π*)/¹(π,σ*). Similarly, the diabatic state on the S₂ PEC was denoted as ¹(n,σ*)/¹(n,π*). The PECs of these adiabatic states calculated at the MS-CASPT2//CAM-B3LYP level and the Mulliken charge populations of *m*- and *p*-AMPD at the CASPT2//CAM-B3LYP level are shown in Figure 2. The PECs of the *m*- and *p*-AMPD diabatic states at the MS-CASPT2//CAM-B3LYP level are shown in Figures 3 and 4, respectively.

Two excited-state minima were located on the S₁ potential energy surface (PES) for both *m*- and *p*-MOB[–] using the TS_{C–C} structure with the A moiety removed for the initial geometry guess. These excited-state minima were denoted *m*- and *p*-CS for *m*- and *p*-MOB[–], respectively, and emit the initial CL. Another set of minima was also located on the S₁ PES using the ground-state *m*- and *p*-MOB[–] structures as the initial

Table 2. The MS-CASPT2 Relative Energies (kcal/mol) of the S_0 and S_1 States and the Energy Gaps (kcal/mol) between the S_1 and S_0 States for m - and p -AMPD Based on the Stationary Points Optimized at the CAM-B3LYP/6-31G Level**

stationary point	MS-CASPT2		
	S_0	S_1	gap (S_1/S_0)
m -Min	0.0	88.4	88.4
m -TS _{O-O}	10.8	29.6	18.8
m -Int _{pos}	13.1	31.8	18.7
m -TS _{C-O-C-O}	10.0	33.1	23.1
m -Int _{neg}	12.2	34.3	22.1
m -TS _{C-C}	12.3	19.2	6.9
p -Min	0.0	94.6	94.6
p -TS _{O-O}	3.7	40.0	36.3
p -Int _{pos}	5.6	32.3	26.7
p -TS _{C-O-C-O}	6.9	32.9	26.0
p -Int _{neg}	6.2	33.1	26.9
p -TS _{C-C}	8.3	16.7	8.3

geometry guess. Similarly, these two excited-state minima were referred to as m -FS and p -FS for m -MOB[−] and p -MOB[−], respectively, because they emit FL. Two adiabatic TSs were also located on the S_1 PES. These TSs, denoted m - and p -TS, are the TSs of the m -CS \leftrightarrow m -FS and p -CS \leftrightarrow p -FS isomerizations, respectively, and were confirmed to be TSs by the vibrational analysis and QSD reaction path following. The important geometric parameters and Mulliken charge populations were summarized in Table 4, and their spectroscopic parameters calculated in the gas phase, DMSO, and water are listed in Tables S1–S3.

DISCUSSION

Below, we will reveal the chemiluminescent mechanisms of m - and p -AMPD. First, the following question will be answered: do their decomposition and excitation processes follow the CIEEL or concerted CT (CT/direct and CTIL) mechanism? Then, the distinction between the CS and FS of AMPPD will be made. Finally, the origin of the odd/even selection rule will be discussed.

1. Chemiluminescent Mechanism of AMPD. 1.1. Chemiluminescent Decomposition of m -AMPD. Three TSs and two Ints were located for the m -AMPD S_0 state via geometry

optimizations by the CAM-B3LYP method. The imaginary vibrational modes indicate that the three TSs correspond to the O₃–O₄ stretch (−2282 cm^{−1}), C₆–O₅–C₂–O₄ twist (−44 cm^{−1}), and C₁–C₂ stretch (−741 cm^{−1}). Therefore, based on the critical geometric parameters of the stationary points in Table 1 and their variation along the IRC in Figure S15, the decomposition of m -AMPD can be divided into three steps (see Figure 1). First, the decomposition is initiated by the O₃–O₄ bond dissociation, which proceeds through the first TS, TS_{O-O} (the O₃–O₄ bond increases by 0.342 Å), to the first Int, Int_{pos}. The C₁–C₂ bond remains intact (it increased by only 0.006 Å) during this step, and the O₃–C₁–C₂–O₄ dihedral angle changes considerably after TS_{O-O} (increases by 21.2° for Int_{pos}), which means the decomposition is not a planar reaction. Second, the C₆–O₅–C₂–O₄ dihedral angle on the **M** moiety gradually rotates through the second TS (TS_{C-O-C-O}, corresponding to the rotation of C₆–O₅–C₂–O₄) to the second Int, Int_{neg}. The C₁–C₂ bond, the O₃–O₄ bond, and the O₃–C₁–C₂–O₄ dihedral angle are slightly perturbed, while the C₆–O₅–C₂–O₄ dihedral angle changes significantly (ca. 60°) during this step. Although the IRC calculation starting from TS_{C-O-C-O} failed due to the very small imaginary frequency, the existence of Int_{pos} and Int_{neg} and the imaginary vibrational mode of TS_{C-O-C-O} clearly indicate that TS_{C-O-C-O} involves the rotation of the C₆–O₅–C₂–O₄ dihedral angle. In the last step, the C₁–C₂ bond begins to dissociate, and the neutral adamantanone molecule and m -MOB[−] are finally produced after the reaction proceeds through the third TS, TS_{C-C}. Therefore, the decomposition of m -AMPD occurs via a typical three-step decomposition mechanism, not an asynchronous, concerted, charge transfer-induced decomposition. This result is different from those for the chemiluminescent decomposition of the previously studied dioxetanone anions.^{16,21,23,24} The NO analyses from the CAM-B3LYP (Figure S1) and SA-CASSCF (Figures S3–S8) calculations show that near the equilibrium structure of m -AMPD, the S_0 state is mainly a closed-shell/¹(σ, σ^*) state, and after the cleavage of the peroxide bond, it changes to the ¹(π, σ^*) state. Then, when the C₁–C₂ bond is broken, it returns to the closed-shell/¹(σ, σ^*) state. The Mulliken charge population also indicates that the negative charge transfers from the **P** moiety to the **M** moiety in the ¹(π, σ^*) state. This indicates that the ¹(π, σ^*) state is a charge transfer state. The occupation numbers of the orbitals calculated at the SA-CASSCF level of theory (Figures S5–

Table 3. The Mulliken Charge Populations of the A, M, and P Moieties in Chart 1 for the Diabatic S_0 and S_1 States Calculated at the CAM-B3LYP//CAM-B3LYP and CASPT2//CAM-B3LYP Levels

stationary point	S_0 /CAM-B3LYP			S_0 /CASPT2			S_1 /CASPT2		
	A	M	P	A	M	P	A	M	P
m -Min	−0.09	−0.13	−0.78	−0.06	−0.10	−0.84	−0.08	−0.11	−0.81
m -TS _{O-O}	−0.25	−0.28	−0.47	−0.06	−0.08	−0.85	−0.39	−0.53	−0.09
m -Int _{pos}	−0.37	−0.46	−0.16	−0.18	−0.57	−0.25	−0.05	−0.11	−0.83
m -TS _{C-O-C-O}	−0.37	−0.46	−0.16	−0.06	−0.11	−0.83	−0.14	−0.40	−0.46
m -Int _{neg}	−0.38	−0.45	−0.17	−0.21	−0.60	−0.20	−0.07	−0.11	−0.83
m -TS _{C-C}	−0.25	−0.56	−0.19	−0.14	−0.52	−0.35	−0.09	−0.34	−0.57
p -Min	−0.11	−0.16	−0.73	−0.08	−0.12	−0.81	−0.06	−0.11	−0.83
p -TS _{O-O}	−0.28	−0.29	−0.43	−0.09	−0.11	−0.79	−0.36	−0.49	−0.15
p -Int _{pos}	−0.35	−0.46	−0.19	−0.11	−0.21	−0.69	−0.15	−0.53	−0.32
p -TS _{C-O-C-O}	−0.36	−0.46	−0.19	−0.11	−0.22	−0.67	−0.16	−0.57	−0.27
p -Int _{neg}	−0.36	−0.45	−0.19	−0.13	−0.22	−0.66	−0.17	−0.57	−0.26
p -TS _{C-C}	−0.25	−0.54	−0.22	−0.14	−0.39	−0.47	−0.09	−0.26	−0.65

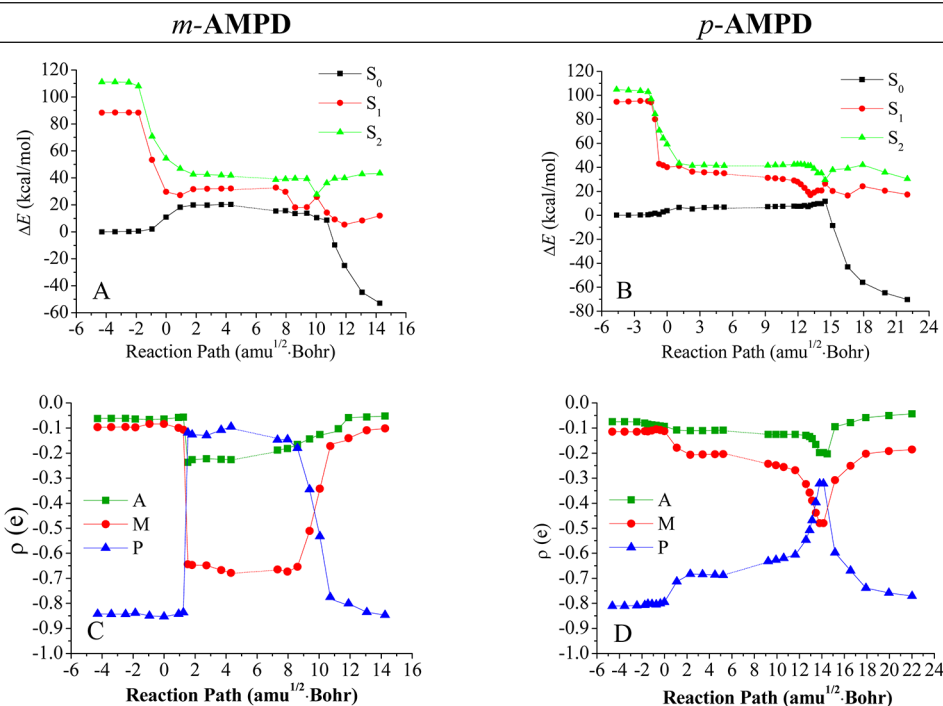


Figure 2. The adiabatic S_0 , S_1 , and S_2 PECs at the MS-CASPT2//CAM-B3LYP level and the Mulliken charge populations of the A, M, and P moieties in Chart 1 for the S_0 state of $m\text{-AMPD}$ and $p\text{-AMPD}$ at the CASPT2//CAM-B3LYP level.

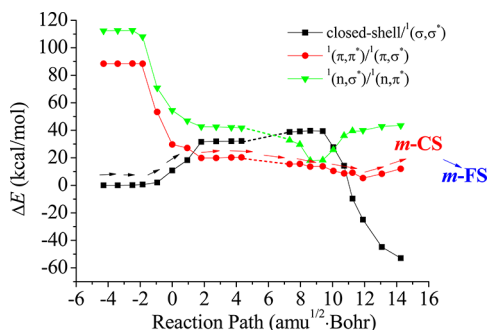


Figure 3. The diabatic PECs calculated by the MS-CASPT2 method using the CAM-B3LYP IRC of $m\text{-AMPD}$.

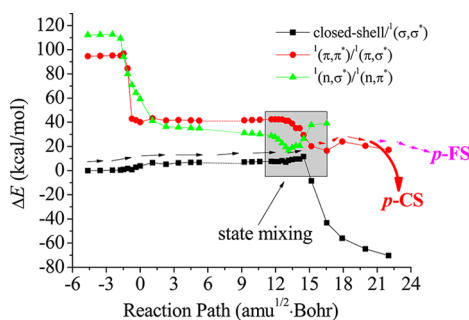


Figure 4. The diabatic PECs calculated by the MS-CASPT2 method using the CAM-B3LYP IRC of $p\text{-AMPD}$.

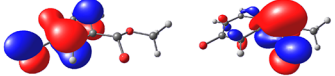
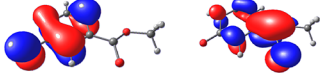
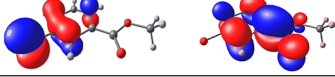
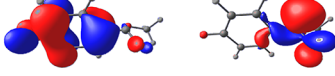
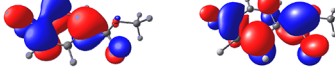
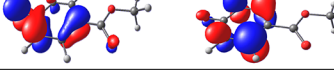
S8) indicate that the CT state is a biradical state in which the $p\text{-}\pi$ conjugation orbital of the phenolic ring and the in-plane p orbital of O_3 are singly occupied, the in-plane p orbital of O_4 is nearly double occupied, and the negative charge primarily resides on O_4 of the M moiety. The similar trends in the variations in the electronic structure (Figure S1) and charge

population (Figure S15C) and in the S_0 PEC (Figure S15A) calculated with the CAM-B3LYP method also proved that the geometric relaxation modeled with DFT is reasonable and qualitatively reliable. The electronic structure variation of the S_0 state is very similar to that for the firefly dioxetanone anion (FDO^-), which implies the double crossing of the closed-shell/ $^1(\sigma,\sigma^*)$ and CT $^1(\pi,\sigma^*)$ states.²⁴ The diabatic electronic PECs in Figure 3 have clearly shown the double crossing of the zero-order diabatic surfaces. From the adiabatic PEC calculated at the MS-CASPT2 level (Figure 2A), we observe that near TS_{O-O} and TS_{C-C} , the S_0 and S_1 surfaces are close to each other (the energy gap is 8.9 and 5.6 kcal/mol at $\text{IRC} = 0.93$ and $10.72 \text{ amu}^{1/2}\cdot\text{Bohr}$, respectively, at the MS-CASPT2 level). This indicates the existence of nonadiabatic transitions near the bond breaking point for O_3-O_4 and C_1-C_2 .

1.2. Chemiluminescent Decomposition of $p\text{-AMPD}$.

According to Figure 1, the PECs (Figure S15 B), the variations in the geometric and electronic structures along the reaction coordinate (Figures S15D and F), and the NO analysis of the stationary points (Figures S1 and S2), the ground-state decomposition of $p\text{-AMPD}$ is nearly the same as that of $m\text{-AMPD}$ based on the CAM-B3LYP calculations. However, both the electronic structure (see Figures S9–S14) and charge population (see Table 3) of the ground state calculated by the MS-CASPT2 method show that the S_0 state is a closed-shell/ $^1(\sigma,\sigma^*)$ state throughout the whole reaction and did not change to the $^1(\pi,\sigma^*)$ state. This result means that the S_0 and S_1 states are not expected to cross during the decomposition process of $p\text{-AMPD}$. The adiabatic PECs at the MS-CASPT2 level indicate that the energy difference between the S_0 and S_1 states is large throughout the whole decomposition. Moreover, the charge population (see Figure 2D) and diabatic PECs (see Figure 4) show that the closed-shell/ $^1(\sigma,\sigma^*)$ and $^1(\pi,\sigma^*)$ states gradually mix with each other upon the cleavage of the C_1-C_2 bond, resulting in the partial CT character of the S_0 state in the

Table 4. The Nearly Singly Occupied Natural Orbitals and the Important Geometric Bond Lengths (Å) and Dihedral Angles (deg) of the *m*- and *p*-MOB[−] CS, FS, and TS between Them Optimized at the SA-CASSCF(10,9)/6-31G** Level (see Figure S16 for Details)

	Singly Occupied NO	C ₂ –O ₄	O ₄ –C ₂ –C ₇ –O ₅	C ₈ –C ₇ –C ₂ –O ₄
<i>m</i> -CS		1.260	-138.3	20.9
<i>m</i> -TS		1.264	-147.8	15.6
<i>m</i> -FS		1.223	-180.0	0.0
<i>p</i> -CS		1.259	-133.5	-63.8
<i>p</i> -TS		1.248	-161.8	7.8
<i>p</i> -FS		1.204	-180.0	0.0

C₁–C₂ cleavage region. At the MS-CASPT2 level, the smallest energy gap between the S₀ and S₁ state is 8.3 kcal/mol at IRC = 13.14 amu^{1/2}·Bohr, which is located in the C₁–C₂ cleavage region. This indicates that the nonadiabatic transfer transition from S₀ to S₁ is more difficult for *p*-AMPD than for *m*-AMPD, which might be another important reason why *m*-AMPD has a much higher CL efficiency than *p*-AMPD.

1.3. Intramolecular CIEEL or Concerted (CT/Direct and CTIL) Mechanism? According to the results discussed in the previous sections, the decomposition of *m*-AMPD is a stepwise process with three TSs and two Ints. First, we conclude that it is not a concerted process before discussing the CT (or ET) and back CT (BCT or BET) phenomena. For the chemiluminescent decomposition of FDO[−], our previous study showed that the intramolecular CIEEL mechanism is invalid because a full single ET did not occur, nor was a radical/anion pair formed during the decomposition; therefore, a gradually reversible CT-initiated luminescence (GRCTIL) mechanism was proposed.²⁴ The situation is very similar for *m*-AMPD. As shown in Figures 2C and S15C and Table 3, the charge population of the ground state indicates that gradual CT and BCT processes occur instead of full one-electron CT processes. No clear radical/anion pair is observed, which is required for the CIEEL mechanism. Thus, the GRCTIL mechanism also applies to the thermolysis of *m*-AMPD, although the decomposition of *m*-AMPD is more complicated than that of FDO[−]. In addition, the solvent-caged radical/anion pair was not found in our calculations. The Mulliken charge population (see Table 3) also shows that the negative charge resides mainly on the M moiety, not on the A moiety, after the O₃–O₄ bond is broken. Moreover, according to the NO analysis (Figures S1 and S3–S8), the singly occupied orbitals of the *m*-AMPD excited state are mainly on O₃ and O₁₀. These results indicate that the intermolecular BCT process of path A assumed by Adam et al.²⁸ is unlikely to occur. The unexpected charge population can be attributed to the electron-withdrawing effect of the methoxy oxygen, O₅. In fact, we found that path B in Scheme 2 is also not entirely valid based on the charge population analysis of the excited product, *m*-CS, which

is directly formed when the C₁–C₂ bond is broken. From the charge population of *m*-CS at the CASPT2 level (see Tables S1–S3), it is obvious that the negative charge still resides on the M moiety and does not transfer back to the P moiety until *m*-CS isomerizes to *m*-FS (see details in the next section). This means the BCT process does not occur during the primary chemiexcitation process; rather, it occurs when the CS is converted into the final fluorophore (FS). As shown in Figures 2D and S15D, the thermolysis of *p*-AMPD is also described by the GRCTIL mechanism, although the decomposition of *p*-AMPD could be different from that of *m*-AMPD. Thus, the intramolecular CIEEL mechanism is invalid and conceptually flawed for the AMPPD CL. Moreover, neither the intramolecular CIEEL nor the CT/direct mechanism can correctly describe the chemiluminescent decomposition of *m*-AMPD and *p*-AMPD.

2. Chemiluminescence and Fluorescence of AMPPD.

CL and FL are two different luminescent phenomena that are often confused in experimental and theoretical studies. In 2011, Roca-Sanjuán et al. characterized the CS and FS of the 2-acetamido-3-methylpyrazine anion, which was used as a small model of the coelenteramide and Cypridina oxyluciferin systems, with the CASSCF/CASPT2 method and established the molecular basis of the differences between the CS and the FS.³⁴ For *m*- and *p*-AMPPD, we found their CS and FS as well as the TS between them using the SA-CASSCF method (see Table 4). However, because the CL and FL emitter should be the same species,^{28,40} the existence of both a CS and FS should be rationalized. *m*- and *p*-CS are the immediate products of the decomposition of *m*- and *p*-AMPD, whereas *m*- and *p*-FS are optimized starting from the Franck–Condon points of the S₀ state of *m*- and *p*-MOB[−], respectively. The *m*- and *p*-CS species can isomerize to *m*- and *p*-FS via *m*- and *p*-TS, respectively, on the adiabatic S₁ PESs. The TSs in these isomerization processes were confirmed by the vibrational analyses and QSD path searches. Compared to *m*- and *p*-FS, *m*- and *p*-CS have obvious CT character, which is demonstrated by the negative charge transfer from the P moiety to the M moiety (see Tables S1–S3). The FL maxima calculated with CASPT2//SA-CASSCF

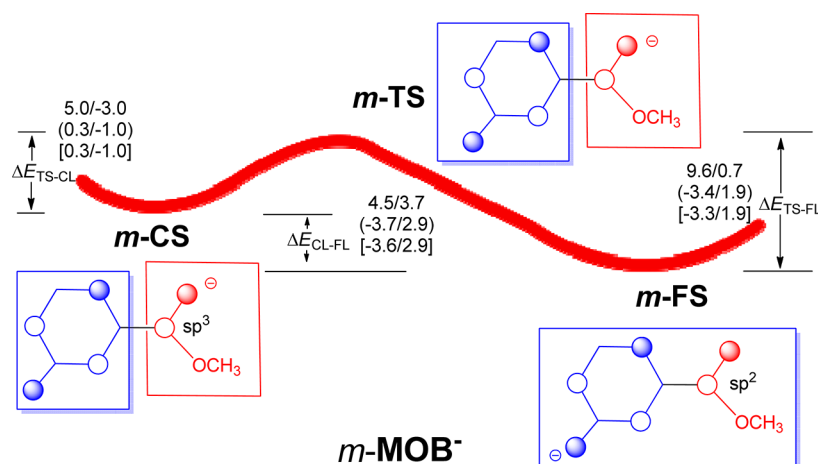


Figure 5. The CASSCF/CASPT2 energy profile (kcal/mol) for the isomerization of *m*-MOB⁻ on the S₁ surface in the gas phase, water (in parentheses), and DMSO (in square brackets) based on the stationary points optimized in the gas phase.

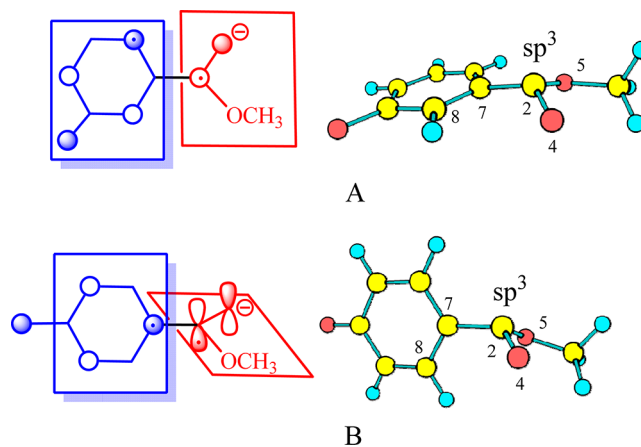
(see Tables S2 and S3) are 435 and 305 nm in water and 431 and 306 nm in DMSO for *m*- and *p*-MOB⁻, respectively. These values agree with those obtained experimentally^{40,65} (415 and 344 nm in water and 466 and 352 nm in DMSO for *m*- and *p*-MOB⁻, respectively). However, the calculated CL maxima, which are 768 and 1136 nm in water and 753 and 1096 nm in DMSO for *m*- and *p*-CL, respectively, do not agree with the experimentally measured maxima given above. Therefore, it is necessary to elucidate the properties of the CS and FS in terms of both the geometric and electronic structures.

The electronic and geometric structures of *m*-CS and *m*-FS differ from each other. As shown by the identities of the singly occupied NO orbitals (in Table 4), *m*-CS mainly corresponds to the electron transfer from the *p*- π conjugated orbital on the phenolic ring (approximately equivalent to the HOMO of phenol) to the π^* orbital of the C₂–O₄ double bond (mainly the *p* orbital of the C₂), while *m*-FS mainly corresponds to the electron transfer from the *p*- π conjugated orbital to the π^* orbital of the phenolic ring (approximately equivalent to the LUMO of phenol). According to the charge population in Tables S1–S3, *m*-CS has CT character as shown by the negative charge transfer from the **P** moiety to the **M** moiety as mentioned previously; however, *m*-FS does not have CT character because its transition is mainly restricted to the phenolic ring. For *m*-CS, a O₄–C₂–C₇–O₅ dihedral angle of -138.3° and a C₂–O₄ bond length of 1.260 Å are indicative of a pyramidal ketone structure, which implies that the C₂ atom is sp³ hybridized. As *m*-CS is isomerized to *m*-FS through *m*-TS, the O₄–C₂–C₇–O₅ dihedral angle becomes planar, resulting in a completely planar *m*-FS structure. In addition, the C₂–O₄ bond length decreases to that of a typical carbonyl (1.227 Å), and the C₂ atom becomes sp² hybridized. The very low barrier ($\Delta E = 5.1, 0.3$, and 0.3 kcal/mol in the gas phase, water, and DMSO, respectively, as calculated with the SA-CASSCF//SA-CASSCF method) indicates that the isomerization from *m*-CS to *m*-FS is facile. It must be noted that the barrier calculated with the CASPT2//SA-CASSCF method is negative ($-3.0, -1.0$, and -1.0 kcal/mol in the gas phase, water, and DMSO, respectively). The negative barrier could be caused by computational errors because the energy and optimization calculations are not performed at the same level. In any case, the isomerization of *m*-CS to *m*-FS is significantly faster than the *m*-CS radiation transition (CL). The *m*-AMPPD CL and *m*-

MOB⁻ FL emitters are the same *m*-FS species, which is consistent with the experimental conclusions.^{40,65} The energy profile of this process was shown in Figure 5.

As shown in Table 4, *p*-CS also mainly corresponds to the electron transfer from the *p*- π conjugated orbital on the phenolic ring to the π^* orbital of the C₂–O₄ double bond, and *p*-FS corresponds to the electron transfer from the *p*- π conjugated orbital to the π^* orbital of the phenolic ring. For *p*-CS, a O₄–C₂–C₇–O₅ dihedral angle of -133.5° and a C₂–O₄ bond length of 1.259 Å are characteristic of a pyramidal structure and sp³ hybridization of C₂, which is similar to the *m*-CS structure. *p*-FS has a planar structure as observed for *m*-FS as well. However, the O₈–C₇–C₂–O₄ dihedral angles of *p*-CS and *m*-CS obviously differ. For *p*-CS, the O₈–C₇–C₂–O₄ dihedral angle of -63.8° indicates that its **M** and **P** planes are almost perpendicular (see Chart 2B), whereas the dihedral

Chart 2. The Optimized Structures of *m*-CS (A) and *p*-CS (B)



angle of 20.9° for *m*-CS indicates that these planes are approximately parallel (Chart 2A). The perpendicular structure of *p*-CS is rather stable, and the isomerization of *p*-CS to *p*-FS is unfavorable. Kinetically, the barrier from *p*-CS to *p*-FS is large (14.2, 16.9, and 16.3 kcal/mol in the gas phase, water, and DMSO, respectively, as calculated using the CASPT2//SA-CASSCF method). Thermodynamically, *p*-CS is lower in energy than *p*-FS (by 9.1, 11.9, and 11.7 kcal/mol in the gas

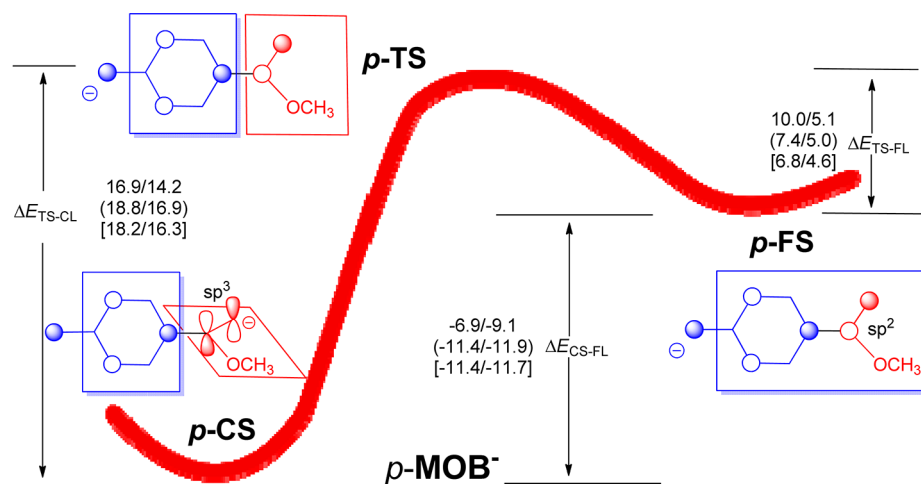
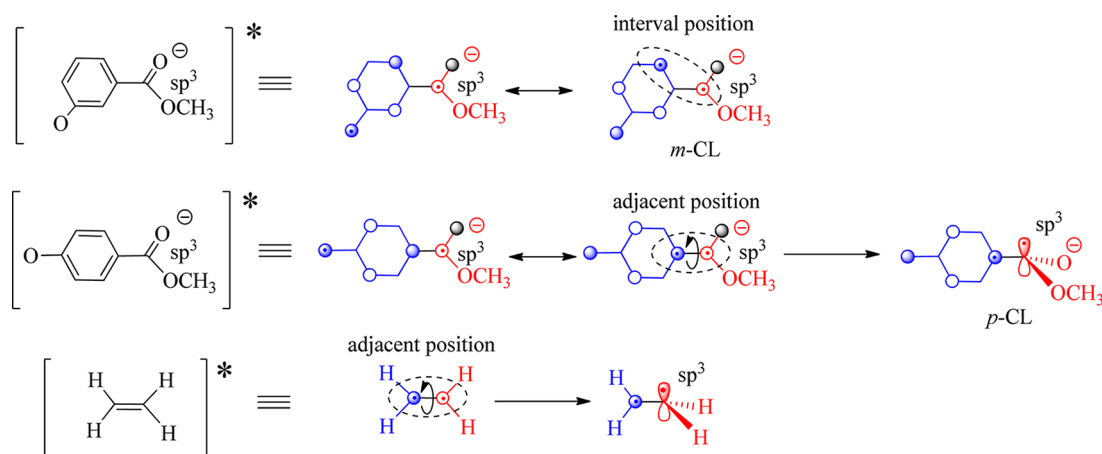


Figure 6. The CASSCF/CASPT2 energy profile (kcal/mol) for the isomerization of $p\text{-MOB}^-$ on the S_1 surface in the gas phase, water (in parentheses), and DMSO (in square brackets) based on the stationary points optimized in the gas phase.

Chart 3. The Resonance Structure and Singly Occupied Orbitals (Red and Blue) for $m\text{-CS}$, $p\text{-CS}$, and the S_1 State of Ethylene



phase, water, and DMSO, respectively, as calculated with CASPT2//SA-CASSCF). Because \mathbf{P} is perpendicular to \mathbf{M} in the $p\text{-CS}$ structure, one can expect that the $p\text{-}\pi$ conjugated orbital on \mathbf{P} is nearly orthogonal to the $\text{C}_2\text{--O}_4 \pi^*$ orbital on \mathbf{M} . This indicates that the rate of the radiation transition from $p\text{-CS}$ to its S_0 state will be very slow according to the Franck–Condon principle. The very low oscillator strength (1.00×10^{-4} , 2.91×10^{-4} , and 1.33×10^{-4} in the gas phase, water, and DMSO, respectively) is consistent with this conclusion. Moreover, the calculated CL maxima of $p\text{-CL}$ (1136 and 1096 nm in water and DMSO, respectively) are in the infrared region, and the internal conversion will be the main deactivation path for $p\text{-CS}$. The difference in the relative positions of the \mathbf{M} and \mathbf{P} planes of $m\text{-}$ and $p\text{-MOB}^-$ might be the most important factor in explaining why the CL efficiency of $p\text{-AMPD}$ is much lower than that of $m\text{-AMPD}$. The energy profile for this process was shown in Figure 6.

The difference in the relative positions of \mathbf{M} and \mathbf{P} between $m\text{-}$ and $p\text{-CS}$ can be attributed to the excited electron–electron repulsion. In $m\text{-CS}$, the two singly occupied orbitals, the $p\text{-}\pi$ conjugation orbital (equivalent to the HOMO of phenol), and the π^* orbital of $\text{C}_2\text{=O}_4$ have positive–negative overlap, and the two singly occupied orbitals are at interval positions, resulting in weak electron–electron repulsion in $m\text{-CL}$. Therefore, the approximate parallel structure is relatively stable

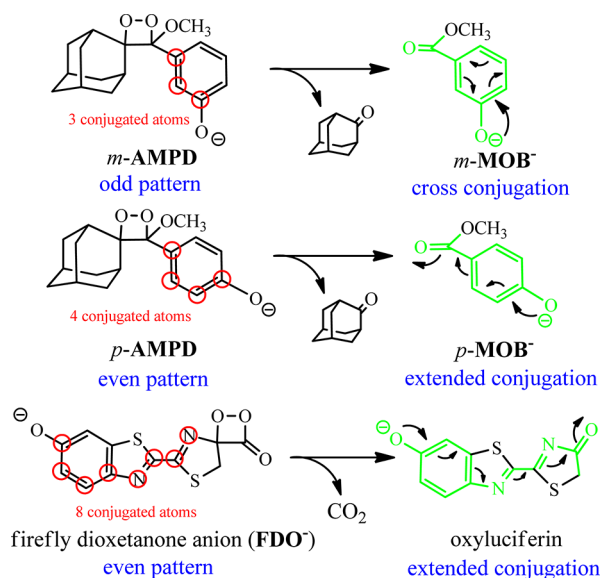
(see Chart 3). On the contrary, if we assume that $p\text{-CS}$ also has an approximately parallel structure like $m\text{-CS}$, the singly occupied $p\text{-}\pi$ conjugation orbital and π^* orbital of $\text{C}_2\text{=O}_4$ are in adjacent positions, which gives rise to strong electron–electron repulsion between the two orbitals. This repulsion causes the rotation of the \mathbf{A} and \mathbf{P} moieties around the $\text{C}_2\text{--C}_7$ bond to produce a perpendicular structure. This is very similar to the rotation around the ethylene double bond in its S_1 state (see Chart 3). In fact, this perpendicularly oriented structure, which corresponds to a local minimum on the S_1 surface and a maximum on the S_0 surface, plays a very important role in nonradiative de-excitation transitions in organic molecules.⁶⁶

3. Essential Insight into the Odd/Even Selection Rule.

Schaap et al. first observed that the *meta*-substituted 1,2-dioxetane, meaning the electron donor was in the *meta* position, exhibits a much higher chemiluminescence efficiency and shorter lifetime than its *para* analog.³⁵ This relationship between the luminescent efficiency and position of the donor group on the aromatic ring was later named the odd/even relationship^{3,37,67} or odd/even selection rule^{18,23} and was also observed for other dioxetanes bearing aromatic-ring substituent, such as adamantyldenedioxetanes^{13,15–17} and bicyclic 1,2-dioxetanes.⁴³ According to the definition of Edwards et al.,³⁷ the odd (even) substitution pattern refers to a 1,2-dioxetane derivative that has an odd (even) number of ring carbon atoms

separating the attachment points of donor group (such as an oxyanion) on the aromatic ring and the four-member ring of 1,2-dioxetane^{37,39} (see Scheme 3). It is generally thought that

Scheme 3. The Odd and Even Patterns of *m*-AMPD, *p*-AMPD, and FDO[−] and Their Corresponding Products

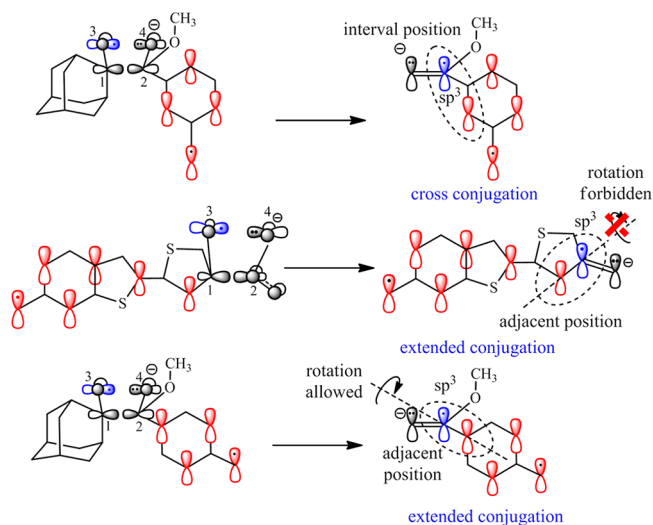


the odd/even selection rule is a result of conjugation effects^{18,23,28,32} and can be extended by alternating the single and double bonds.^{3,68} Therefore, the odd pattern of *m*-AMPD leads to a cross conjugation^{69,70} product such as *m*-MOB[−], while the even pattern of *p*-AMPD results in an extended conjugation product such as *p*-MOB[−]. According to this definition, FDO[−] should be considered to have an even pattern because it has an even number (eight) of conjugated atoms and produces an oxyluciferin with extended conjugation (see Scheme 3). Therefore, the FDO[−] CL efficiency should be low. However, the firefly BL has the most efficient CL known at the present time.⁷¹ This indicates that the odd/even selection rule might be based on other effects in addition to the conjugation effects related to the substituent positions. The origin of the odd/even selection rule should be reconsidered. Below we reconsider the odd/even selection rule for the CL efficiency by qualitatively comparing the current computational results for AMPD with our previous computational results for FDO[−].²⁴ According to our above calculations, the final chemiluminescence (singlet state) yields (Φ^{CL}) of *m*- and *p*-AMPD are directly proportional to the product of the initial CS yield (Φ^{CS}), the efficiency of the transformation (Φ^{trans}) from the initial CS to the final fluorophore (FS for both *m*- and *p*-AMPD), and the fluorescence yield (Φ^{FL}) of the final fluorophore.

3.1. Initial CS Yield. Double crossings between the diabatic $^1(\sigma, \sigma^*)$ and $^1(\pi, \sigma^*)$ states are observed in the chemiluminescent decompositions of both *m*-AMPD (Figure 3) and FDO[−] (Figure 5 in ref 24) but not in that of *p*-AMPD (Figure 4). The crossings between the $^1(\sigma, \sigma^*)$ and $^1(\pi, \sigma^*)$ states allow for the nonadiabatic transition from *S*₀ to *S*₁, which leads to the high chemiexcitation efficiency. Due to the electron-withdrawing inductive effect of the methoxy group on *m*- and *p*-AMPD, the singly occupied p orbital of the peroxide bond and the p- π conjugation orbital of the aromatic ring are on different sides of the 1,2-dioxetane ring during its decomposition (on the C₁–O₃

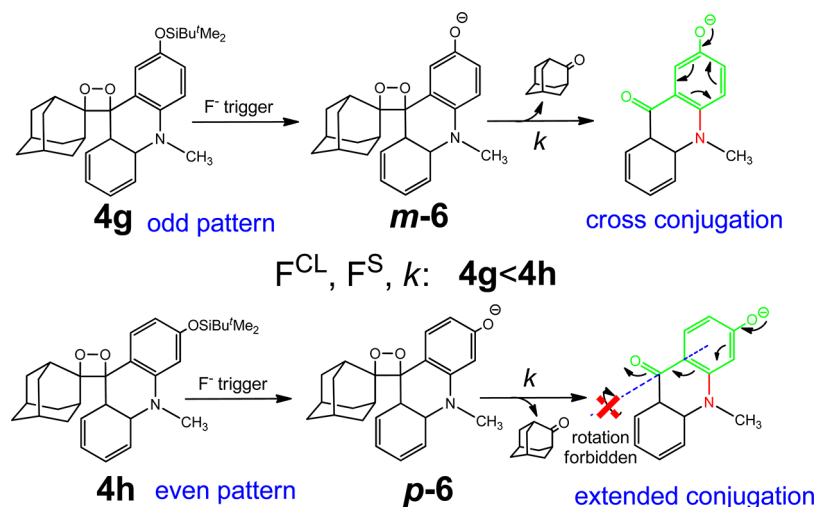
and C₂–O₄ sides, respectively; see Scheme 4). According to the calculations (see Figures 3 and 4), the PES crossings between

Scheme 4. The Singly Occupied Orbitals (Red and Blue) of 1,2-Dioxetanes with Different Substitution Patterns (*m*-AMPD, *p*-AMPD, and FDO[−]) and Their Corresponding Products (*m*-MOB[−], *p*-MOB[−], and the Oxyluciferin Anion, Respectively)



the $^1(\sigma, \sigma^*)$ and $^1(\pi, \sigma^*)$ states can occur more easily for odd-pattern derivatives (*m*-AMPD) than for even-pattern derivatives (*p*-AMPD). However, this conclusion is not always correct. For FDO[−], the strong electronegativity of the carbonyl oxygen of the CO₂ moiety, which is on the opposite side of the 1,2-dioxetanone ring from the aromatic ring, forces the singly occupied p orbital of the peroxide bond and the singly occupied p- π conjugation orbital of the aromatic ring to be on the same side of the 1,2-dioxetane ring during its decomposition (both on the C₁–O₃ side). Although the oxyluciferin product of the FDO[−] chemiluminescence undoubtedly has an even pattern (extended conjugation), FDO[−] actually decomposes in a manner similar to *m*-AMPD (see Scheme 4). This implies that the chemiexcitation efficiency cannot be predicted simply by the position of the substituent. The odd/even rule is only correct for 1,2-dioxetanes with the electron-withdrawing group and the aromatic ring attached to the same carbon atom of the 1,2-dioxetane ring, for example, AMPPD. Because most experimental observations are based on the decomposition of adamantane-substituted or bicyclic 1,2-dioxetanes^{28,37–42,72–81} in which the electron-withdrawing group and aromatic ring are attached to the same carbon atom of the 1,2-dioxetane ring, their chemiexcitation efficiencies obey the odd/even selection rule. On the basis of the experimental observations of this type of dioxetane, the odd/even rule was proposed.^{3,18,23,37,67} However, 1,2-dioxetanones such as FDO[−] whose electron-withdrawing group and aromatic ring are attached to different carbon atoms of the 1,2-dioxetane ring will violate this rule. The 1,2-dioxetanes without explicit electron-withdrawing groups, such as **4g** and **4h**, which are derived from 9-adamantylideneacridanes⁸² do not follow the odd/even selection rule (see Scheme 5). In fact, experimental observations showed that **4h** (even pattern) has a larger thermolysis rate constant and a higher singlet excitation yield than **4g** (odd pattern). There could be another type of 1,2-

Scheme 5. The Chemiluminescence of the Spiroacridane Spiroadamantane Dioxetanes

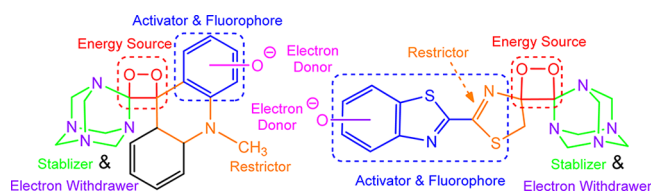


dioxetane which does not follow the odd/even selection rule. They have two electron-withdrawing substituents of similar strength on different sides of the 1,2-dioxetane ring during its decomposition.

3.2. Transformation Efficiency from the Initial CS to the Final Fluorophore. As discussed in section 2, the even-pattern derivatives such as *p*-AMPD will generate a perpendicular CS similar to *p*-CS due to the electron–electron repulsion after the chemiexcitation process. This perpendicular CS is rather stable, and the isomerization yield from CS to FS is very low. Similarly, because oxyluciferin is an even-pattern product, one might expect the two singly occupied orbitals of its CS to have a perpendicular orientation (see Chart 3 and Scheme 4). However, the rigid structure of the cyclic ketone in oxyluciferin restricts the rotation of the carbonyl group around the C–N bond (see Scheme 4), preventing the formation of the perpendicular CS. Thus, the FS can be produced directly and efficiently, which explains the absence of an independent CS (with an sp^3 carbon on the carbonyl group) for oxyluciferin.⁸³ Therefore, FDO^- directly decomposes into the final fluorophore with a high Φ^{CL} , even though it is an even-pattern 1,2-dioxetane derivative. Furthermore, this steric effect can also explain the violation of the odd/even selection rule by **4g** and **4h**. Their FSs are rigid cyclic ketones, which restrict the rotation of the carbonyl group around the C–C bond (see Scheme 5).

In summary, the previously proposed odd/even selection rule is not applicable to all 1,2-dioxetanes whose chemiluminescence is induced by intramolecular CT. This rule originates from the electron–electron interactions in the chemiexcitation process, which result from the conjugation effect of the substituent on the aromatic ring and the inductive effect of the substituent on the 1,2-dioxetane ring. The electron–electron interactions are strongly affected by steric effects. Therefore, the combination of electron-withdrawing, conjugation, and steric effects must be considered in the design of a high-performance CL system. On the basis of the combined effects, we theoretically design some urotropine-substituted 1,2-dioxetanes (see Chart 4) and expect that they exhibit both the stability of **AMPPD** and the efficiency of firefly chemiluminescence.

Chart 4. Designed Urotropine-Substituted 1,2-Dioxetanes



CONCLUSIONS

To solve the three critical problems of the **AMPPD** CL mechanism, we studied the complete CL mechanism from the decomposition of **AMPD** to the formation of the final fluorophore for the first time using a combination of density functional theory and multiconfigurational methods.

For the thermolysis of *m*-AMPD, a three-step CT-induced decomposition process was found. Zero-order double crossings between the $^1(\sigma, \sigma^*)$ and $^1(\pi, \sigma^*)$ states were predicted to occur during the decomposition. The primary chemiexcitation during the decomposition can be attributed to the preferred nonadiabatic transition of the double crossings. For the thermolysis of *p*-AMPD, state mixing was observed in the C–C cleavage region instead of the double crossings between the $^1(\sigma, \sigma^*)$ and $^1(\pi, \sigma^*)$ states. Therefore, the chemiexcitation of *p*-AMPD is much more difficult than that of *m*-AMPD.

After the initial chemiexcitation process, two Mins (*m*- and *p*-CS) on the S_1 surface would form before the final fluorophores (*m*- and *p*-FS) for *m*- and *p*-AMPD, respectively. *m*-CS is unstable and rapidly isomerizes to *m*-FS, preventing the detection of the *m*-CS emission. In contrast, *p*-CS, which has a perpendicular structure, is rather stable and hardly isomerizes to *p*-FS. The *p*-CS emission efficiency, however, is very low because of its perpendicular structure. The different stabilities of *m*- and *p*-CS cause the dramatic difference in Φ^{CL} between *m*- and *p*-AMPPD.

Furthermore, we also found that the odd/even relationship between the CL efficiency and the position of the donor on the aromatic cycle is determined not only by the substitution on the aromatic ring but also by the substitution on the 1,2-dioxetane ring itself. The electron–electron interactions due to conjugation and inductive effects are the origin of the odd/even selection rule. Moreover, steric effects also play an important role in the odd/even selection rule. The combination of

conjugation, inductive, and steric effects should be considered in the design of high-performance dioxetane CL systems.

■ ASSOCIATED CONTENT

■ Supporting Information

Natural orbitals and occupation numbers at the CAM-B3LYP level and active pseudonatural orbitals and occupation numbers at the SA-CASSCF level; S_0 PECs, variations in the Mulliken charge population and important geometric parameters at the CAM-B3LYP level along the IRCs of *m*- and *p*-AMPD; activation energies and spectroscopic data for the key structures of *m*- and *p*-MOB in the gas phase, water, and DMSO at the CASPT2//SA-CASSCF level; Cartesian coordinates for the key structures of AMPD and MOB optimized at the CAM-B3LYP and SA-CASSCF levels, respectively. This material is available free of charge via the Internet at <http://pubs.acs.org>.

■ AUTHOR INFORMATION

Corresponding Author

*E-mail: yajun.liu@bnu.edu.cn (Y.-J. L.).

Notes

The authors declare no competing financial interest.

■ ACKNOWLEDGMENTS

This work was supported by grants from the National Natural Science Foundation of China (Grant Nos. 21073017 and 21273021) and the Major State Basic Research Development Programs (Grant No. 2011CB808500).

■ REFERENCES

- (1) Beck, S.; Koster, H. *Anal. Chem.* **1990**, *62*, 2258.
- (2) Adam, W.; Reinhardt, D.; Saha-Möller, C. R. *Analyst* **1996**, *121*, 1527.
- (3) Matsumoto, M. *J. Photochem. Photobiol., C* **2004**, *5*, 27.
- (4) Adam, W.; Kazakov, D. V.; Kazakov, V. P. *Chem. Rev.* **2005**, *105*, 3371.
- (5) Mayer, A.; Neuenhofer, S. *Angew. Chem., Int. Ed.* **1994**, *33*, 1044.
- (6) Voyta, J. C.; Edwards, B.; Bronstein, I. *Clin. Chem.* **1988**, *34*, 1157.
- (7) Bronstein, I.; Edwards, B.; Voyta, J. C. *J. Biolumin. Chemilumin.* **1989**, *4*, 99.
- (8) Bronstein, I.; McGrath, P. *Nature* **1989**, *338*, 599.
- (9) Bronstein, I.; Voyta, J. C.; Edwards, B. *Anal. Biochem.* **1989**, *180*, 95.
- (10) Schuster, G. B.; Turro, N. J.; Steinmetzer, H. C.; Schaap, A. P.; Faler, G.; Adam, W.; Liu, J. C. *J. Am. Chem. Soc.* **1975**, *97*, 7110.
- (11) Bronstein, I.; Kricka, L. J. *J. Clin. Lab. Anal.* **1989**, *3*, 316.
- (12) Beck, S.; O'Keeffe, T.; Coull, J. M.; Köster, H. *Nucleic Acids Res.* **1989**, *17*, 5115.
- (13) Bronstein, I.; Voyta, J. C.; Thorpe, G. H.; Kricka, L. J.; Armstrong, G. *Clin. Chem.* **1989**, *35*, 1441.
- (14) Bartoloni, F. H.; de Oliveira, M. A.; Augusto, F. A.; Ciscato, L. F. M. L.; Bastos, E. L.; Baader, W. J. *J. Braz. Chem. Soc.* **2012**, *23*, 2093.
- (15) Vico, L. D.; Liu, Y.-J.; Krogh, J. W.; Lindh, R. *J. Phys. Chem. A* **2007**, *111*, 8013.
- (16) Liu, F.; Liu, Y.-J.; Vico, L. D.; Lindh, R. *Chem. Phys. Lett.* **2009**, *484*, 69.
- (17) Reguero, M.; Bernardi, F.; Bottoni, A.; Olivucci, M.; Robb, M. A. *J. Am. Chem. Soc.* **1991**, *113*, 1566.
- (18) Takano, Y.; Tsunesada, T.; Isobe, H.; Yoshioka, Y.; Yamaguchi, K.; Saito, I. *Bull. Chem. Soc. Jpn.* **1999**, *72*, 213.
- (19) Tanaka, C.; Tanaka, J. *J. Phys. Chem. A* **2000**, *104*, 2078.
- (20) Wilsey, S.; Bernardi, F.; Olivucci, M.; Robb, M. A.; Murphy, S.; Adam, W. *J. Phys. Chem. A* **1999**, *103*, 1669.
- (21) Isobe, H.; Yamanaka, S.; Okumura, M.; Yamaguchi, K. *J. Phys. Chem. A* **2009**, *113*, 15171.
- (22) Liu, F.; Liu, Y.-J.; Vico, L. D.; Lindh, R. *J. Am. Chem. Soc.* **2009**, *131*, 6181.
- (23) Isobe, H.; Takano, Y.; Okumura, M.; Kuramitsu, S.; Yamaguchi, K. *J. Am. Chem. Soc.* **2005**, *127*, 8667.
- (24) Yue, L.; Liu, Y.-J.; Fang, W.-H. *J. Am. Chem. Soc.* **2012**, *134*, 11632.
- (25) Yue, L.; Roca-Sanjuán, D.; Lindh, R.; Ferré, N.; Liu, Y.-J. *J. Chem. Theory Comput.* **2012**, *8*, 4359.
- (26) Trofimov, A. V.; Mielke, K.; Vasil'ev, R. F.; Adam, W. *Photochem. Photobiol.* **1996**, *63*, 463.
- (27) Koo, J.-Y.; Schuster, G. B. *J. Am. Chem. Soc.* **1977**, *99*, 6107.
- (28) Adam, W.; Trofimov, A. V. *J. Org. Chem.* **2000**, *65*, 6474.
- (29) Adam, W.; Bronstein, I.; Trofimov, A. V.; Vasil'ev, R. F. *J. Am. Chem. Soc.* **1999**, *121*, 958.
- (30) Catalani, L. H.; Wilson, T. *J. Am. Chem. Soc.* **1989**, *111*, 2633.
- (31) McCapra, F. *J. Photochem. Photobiol., A* **1990**, *51*, 21.
- (32) McCapra, F. *Tetrahedron Lett.* **1993**, *34*, 6941.
- (33) Wilson, T. *Photochem. Photobiol.* **1995**, *62*, 601.
- (34) Roca-Sanjuán, D.; Delcey, M. G.; Navizet, I.; Ferré, N.; Liu, Y.-J.; Lindh, R. *J. Chem. Theory Comput.* **2011**, *7*, 4060.
- (35) Schaap, A. P.; Chen, T.-S.; Handley, R. S.; DeSilva, R.; Giri, B. P. *Tetrahedron Lett.* **1987**, *28*, 1155.
- (36) Matsumoto, M.; Suganuma, H.; Azami, M.; Aoshima, N.; Mutoh, H. *Heterocycles* **1995**, *41*, 2419.
- (37) Edwards, B.; Sparks, A.; Voyta, J. C.; Bronstein, I. *J. Biolumin. Chemilumin.* **1990**, *5*, 1.
- (38) Edwards, B.; Sparks, A.; Voyta, J. C.; Strong, R.; Murphy, O.; Bronstein, I. *J. Org. Chem.* **1990**, *55*, 6225.
- (39) Matsumoto, M.; Watanabe, N.; Kobayashi, H.; Azami, M.; Ikawa, H. *Tetrahedron Lett.* **1997**, *38*, 411.
- (40) Adam, W.; Bronstein, I.; Trofimov, A. V. *J. Phys. Chem. A* **1998**, *102*, 5406.
- (41) Watanabe, N.; Kobayashi, H.; Azami, M.; Matsumoto, M. *Tetrahedron* **1999**, *55*, 6831.
- (42) Matsumoto, M.; Hiroshima, T.; Chiba, S.; Isobe, R.; Watanabe, N.; Kobayashi, H. *Luminescence* **1999**, *14*, 345.
- (43) Hoshiya, N.; Fukuda, N.; Maeda, H.; Watanabe, N.; Matsumoto, M. *Tetrahedron* **2006**, *62*, 5808.
- (44) Tanaka, C.; Tanaka, J.; Matsumoto, M. *Phys. Chem. Chem. Phys.* **2011**, *13*, 16005.
- (45) Yanai, T.; Tew, D. P.; Handy, N. C. *Chem. Phys. Lett.* **2004**, *393*, 51.
- (46) Rudberg, E.; Salek, P.; Helgaker, T.; Ågren, H. *J. Chem. Phys.* **2005**, *123*, 184108.
- (47) Peach, M. J. G.; Helgaker, T.; Salek, P.; Keal, T. W.; Lutnæs, O. B.; Tozer, D. J.; Handy, N. C. *Phys. Chem. Chem. Phys.* **2006**, *8*, 558.
- (48) Gonzalez, C.; Schlegel, H. B. *J. Chem. Phys.* **1989**, *90*, 2154.
- (49) Gonzalez, C.; Schlegel, H. B. *J. Phys. Chem.* **1990**, *94*, 5523.
- (50) Hehre, W. J.; Ditchfield, R.; Pople, J. A. *J. Chem. Phys.* **1972**, *56*, 2257.
- (51) Hariharan, P. C.; Pople, J. A. *Theor. Chim. Acta* **1973**, *28*, 213.
- (52) Andersson, K.; Malmqvist, P.-Å.; Roos, B. O. *J. Chem. Phys.* **1992**, *96*, 1218.
- (53) Finley, J.; Malmqvist, P.-Å.; Roos, B. O.; Serrano-Andrés, L. *Chem. Phys. Lett.* **1998**, *288*, 299.
- (54) Andersson, K.; Malmqvist, P. A.; Roos, B. O.; Sadlej, A. J.; Wolinski, K. *J. Phys. Chem.* **1990**, *94*, 5483.
- (55) Roos, B. O.; Taylor, P. R.; Siegbahn, P. E. M. *Chem. Phys.* **1980**, *48*, 157.
- (56) Siegbahn, P.; Heiberg, A.; Roos, B.; Levy, B. *Phys. Scr.* **1980**, *21*, 323.
- (57) Roos, B. O.; Lindh, R.; Malmqvist, P.-Å.; Veryazov, V.; Widmark, P.-O. *J. Phys. Chem. A* **2003**, *108*, 2851.
- (58) Frisch, M. J.; Trucks, G. W.; Schlegel, H. B.; Scuseria, G. E.; Robb, M. A.; Cheeseman, J. R.; Scalmani, G.; Barone, V.; Mennucci, B.; Petersson, G. A.; Nakatsuji, H.; Caricato, M.; Li, X.; Hratchian, H. P.; Izmaylov, A. F.; Bloino, J.; Zheng, G.; Sonnenberg, J. L.; Hada, M.;

Ehara, M. T.; K.; Fukuda, R.; Hasegawa, J.; Ishida, M.; Nakajima, T.; Honda, Y.; Kitao, O.; Nakai, H.; Vreven, T.; Montgomery, J. A., Jr.; Peralta, J. E.; Ogliaro, F.; Bearpark, M.; Heyd, J. J.; Brothers, E.; Kudin, K. N.; Staroverov, V. N.; Kobayashi, R.; Normand, J.; Raghavachari, K.; Rendell, A.; Burant, J. C.; Iyengar, S. S.; Tomasi, J.; Cossi, M.; Rega, N.; Millam, N. J.; Klene, M.; Knox, J. E.; Cross, J. B.; Bakken, V.; Adamo, C.; Jaramillo, J.; Gomperts, R.; Stratmann, R. E.; Yazyev, O.; Austin, A. J.; Cammi, R.; Pomelli, C.; Ochterski, J. W.; Martin, R. L.; Morokuma, K.; Zakrzewski, V. G.; Voth, G. A.; Salvador, P.; Dannenberg, J. J.; Dapprich, S.; Daniels, A. D.; Farkas, Ö.; Foresman, J. B.; Ortiz, J. V.; Cioslowski, J.; Fox, D. J. *Gaussian 09*, revision A.02; Gaussian, Inc.: Wallingford, CT, 2009.

(59) Aquilante, F.; De Vico, L.; Ferré, N.; Ghigo, G.; Malmqvist, P.-Å.; Neogrády, P.; Pedersen, T. B.; Pitoňák, M.; Reiher, M.; Roos, B. O.; Serrano-Andrés, L.; Urban, M.; Veryazov, V.; Lindh, R. *J. Comput. Chem.* **2010**, *31*, 224.

(60) Sun, J.-Q.; Ruedenberg, K. *J. Chem. Phys.* **1993**, *99*, 5257.

(61) Sun, J.-Q.; Ruedenberg, K. *J. Chem. Phys.* **1993**, *99*, 5269.

(62) Cossi, M.; Rega, N.; Scalmani, G.; Barone, V. *J. Comput. Chem.* **2003**, *24*, 669.

(63) Werner, H. J.; Knowles, P. J.; Knizia, G.; Manby, F. R.; Schütz, M.; Celani, P.; Korona, T.; Lindh, R.; Mitrushenkov, A.; Rauhut, G.; Shamasundar, K. R.; Adler, T. B.; Amos, R. D.; Bernhardsson, A.; Berning, A.; Cooper, D. L.; Deegan, M. J. O.; Dobbyn, A. J.; Eckert, F.; Goll, E.; Hampel, C.; Hesselmann, A.; Hetzer, G.; Hrenar, T.; Jansen, G.; Köppl, C.; Liu, Y.; Lloyd, A. W.; Mata, R. A.; May, A. J.; McNicholas, S. J.; Meyer, W.; Mura, M. E.; Nicklass, A.; O'Neill, D. P.; Palmieri, P.; Pflüger, K.; Pitzer, R.; Reiher, M.; Shiozaki, T.; Stoll, H.; Stone, A. J.; Tarroni, R.; Thorsteinsson, T.; Wang, M.; Wolf, A. *MOLPRO*, version 2010.1; Cardiff University: Cardiff, U. K.; Universität Stuttgart: Stuttgart, Germany, 2010.

(64) Aquilante, F.; De Vico, L.; Ferré, N.; Ghigo, G.; Malmqvist, P. Å.; Neogrády, P.; Pedersen, T. B.; Pitoňák, M.; Reiher, M.; Roos, B. O.; Serrano-Andrés, L.; Urban, M.; Veryazov, V.; Lindh, R. *J. Comput. Chem.* **2010**, *31*, 224.

(65) Tu, L.; Wang, Y.; Yang, Y.; Bakker, B. H.; Kong, X.; Brouwer, A. M.; Buma, W. J.; Zhang, H. *Phys. Chem. Chem. Phys.* **2010**, *12*, 6789.

(66) Sharafy, S.; Muszkat, K. A. *J. Am. Chem. Soc.* **1971**, *93*, 4119.

(67) Matsumoto, M.; Kakuno, F.; Kikkawa, A.; Hoshiya, N.; Watanabe, N.; Ijuin, H. K. *Tetrahedron Lett.* **2009**, *50*, 2337.

(68) Matsumoto, M.; Ishihara, T.; Watanabe, N.; Hiroshima, T. *Tetrahedron Lett.* **1999**, *40*, 4571.

(69) Limacher, P. A.; Lüthi, H. P. *WIREs Comput. Mol. Sci.* **2011**, *1*, 477.

(70) Phelan, N. F.; Orchin, M. *J. Chem. Educ.* **1968**, *45*, 633.

(71) Ando, Y.; Niwa, K.; Yamada, N.; Enomoto, T.; Irie, T.; Kubota, H.; Ohmiya, Y.; Akiyama, H. *Nat. Photonics* **2008**, *2*, 44.

(72) Matsumoto, M.; Yamada, K.; Watanabe, N.; Ijuin, H. K. *Luminescence* **2007**, *22*, 420.

(73) Matsumoto, M.; Suzuki, H.; Sano, Y.; Watanabe, N.; Ijuin, H. K. *Tetrahedron Lett.* **2008**, *49*, 5372.

(74) Matsumoto, M.; Tanimura, M.; Akimoto, T.; Watanabe, N.; Ijuin, H. K. *Tetrahedron Lett.* **2008**, *49*, 4170.

(75) Tanimura, M.; Watanabe, N.; Ijuin, H. K.; Matsumoto, M. *J. Org. Chem.* **2010**, *75*, 3678.

(76) Watanabe, N.; Kikuchi, M.; Maniwa, Y.; Ijuin, H. K.; Matsumoto, M. *J. Org. Chem.* **2010**, *75*, 879.

(77) Watanabe, N.; Sano, Y.; Suzuki, H.; Tanimura, M.; Ijuin, H. K.; Matsumoto, M. *J. Org. Chem.* **2010**, *75*, 5920.

(78) Matsumoto, M.; Suzuki, H.; Watanabe, N.; Ijuin, H. K.; Tanaka, J.; Tanaka, C. *J. Org. Chem.* **2011**, *76*, 5006.

(79) Tanimura, M.; Watanabe, N.; Ijuin, H. K.; Matsumoto, M. *J. Org. Chem.* **2011**, *76*, 902.

(80) Tanimura, M.; Watanabe, N.; Ijuin, H. K.; Matsumoto, M. *J. Org. Chem.* **2012**, *77*, 4725.

(81) Watanabe, N.; Kino, H.; Watanabe, S.; Ijuin, H. K.; Yamada, M.; Matsumoto, M. *Tetrahedron* **2012**, *68*, 6079.

(82) Adam, W.; Reinhardt, D. *J. Chem. Soc., Perkin Trans. 2* **1997**, 1453.

(83) Navizet, I.; Roca-Sanjuán, D.; Yue, L.; Liu, Y.-J.; Ferré, N.; Lindh, R. *Photochem. Photobiol.* **2013**, *89*, 319.

NOTE ADDED AFTER ASAP PUBLICATION

This article was published ASAP on April 24, 2013. Reference 64 has been modified. The corrected version was published on April 26, 2013.